

Dear Dr Kirilova and coauthors,

I have now carefully read your revised paper and also considered James Gilgannon's review of that version of your manuscript and came to the conclusion that, in its current form, the manuscript is not yet ready to be published in SE.

I do think though that with a rework that addresses the concerns, your paper will make a robust and well-cited contribution, and I look forward to receiving your revised version.

Best regards,
Florian Füsseis

Dear Dr Füsseis,

We are very grateful for your time and constructive feedback. We acknowledge your expertise in porosity analyses and CT-data interpretation. Our interest is to produce a valuable contribution to the scientific society, thus we have carefully considered all of your comments. Please find our responses in green text below.

Kind Regards,
Martina Kirilova
On behalf of co-authors:
Virginia Toy, Katrina Sauer, François Renard, Klaus Gessner, Richard Wirth, and Xianghui Xiao

I see a certain disconnect between the data you present and your discussion, in particular Section 5.3, in particular, it isn't obvious to me that your data really support the conclusions you draw there. This doesn't mean that the conclusions are incorrect, but rather that the trends in the data you report are not overly obvious.

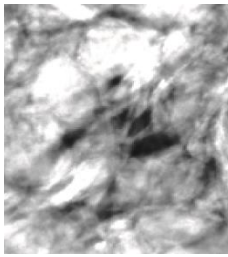
In particular, I have concerns about the validity of the shape analysis, which hinges entirely on the covariance matrix. The matrix really describes the shape of an ellipsoid, not a pore. I would argue that for the conclusions to be robust, one would need to demonstrate that the eigenvalues/vectors indeed are a good representation of pore shapes. Pores in deformed rocks can have very convoluted shapes which are difficult to describe with standard mathematical operations. There are, however, more sophisticated tools, such as Minkowski functionals, which you could use.

Response:

We realize that it is possible to characterize shapes of non-ellipsoidal features using more complex methods than fitted ellipsoids. However, it is not true that the covariance matrix approximates the pores as ellipses. Instead, the covariance matrix can be calculated on any shape. For an ellipse, the 3 eigenvalues will represent exactly the 3 axis of the ellipse. For more complicated shapes, the 3 eigenvalues measure length scales of the object in 3 perpendicular directions of space. In addition, pores detected in our samples are predominantly ellipsoidal (see figure below).

Furthermore, fitting ellipsoids is a standard and widely employed method in the field of porosity analysis. For example, Menegon et al., (2015) used fitted ellipsoids to estimate the length of the longest axis of pores in monzonite ultramylonites. The editor is a co-author of this manuscript. This means our data are easily compared to measurements made in prior studies. In addition, Sufian et al., (2018) noted that their pore orientation tensor (which is the eigenvectors of a fitted ellipsoid) is of a similar form to

the Minkowski interface tensor. Thus, we do not think that undertaking the analysis with Minkowski functionals as recommended will substantially change our results. We have not performed a new analysis.



Ellipsoidal pores in sample DFD-1B 69_2.54 (Fig 8a in the manuscript)

My second major concern arises from the polynomial fitting - where really the R^2 values aren't too great. I suspect, on the basis of my own experience, that you could yield substantially different porosity values quite easily if you used slightly different fits.

Response:

We acknowledge the concern that R^2 values are “not too good”. The method we used is designed to estimate and exclude fractures within the sample data, which means the R^2 will be low. We can observe microfractures present even at small volumes and this method allows us to estimate when those fractures begin to adversely affect a total porosity calculation. We are not optimizing for R^2 , we are biasing the fit to smaller volumes where more pores exist, and biasing the fit against higher pore volumes where more fractures exist. A consequence of this is that the R^2 values are lower, but we believe it results in a more accurate estimate of total porosity excluding fractures.

Specific comments (line numbers)

98 I think it might be helpful if you very briefly, as obviously described in detail elsewhere, mentioned how these samples are related to the activity of the fault. A figure (BSE images and corresponding slices through uCT data) showing the microfabrics of the four samples should be added (and can replace some of Figs 1 and 2). Also, mineral compositions, grain sizes and proportions should be reported in a table. This is relevant for your section 5.2 below.

Response:

Section 5.2 discusses our data in the context of published studies where all the information required by the editor is described in detail. However, images of the samples are available as part of an unpublished PhD thesis (it is currently in final revision stage). We could include them but would then want to add the student's name to our author list. Is that an acceptable solution?

103 Please report on the sample-detector distance, as this is important to estimate a possible phase contrast in the data.

Response:

The sample detector distance was 70 mm. Information added in line 105.

103 The sample size is only of minor relevance here, since the field of view will only be just over 2 mm high at 10x magnification (which I believe gives 1.3 μm voxel size). What is the widths of your FoV?

Response:

The width of FOV was 2.81 mm. Information added in line 105.

106 Why no phase retrieval in reconstruction?

Response:

These samples were analyzed in 2011 before such methods were implemented at APS.

111 What are the dimensions of the sub-samples, how did you choose them, and are they statistically relevant?

Response:

The subsamples were cropped from representative areas of the whole sample that show typical mineral associations and porosity distribution within a sample. The size of the sub-samples ranges between 601^3 voxels and 801^3 voxels. Differences in the sub-sample sizes depend on the quality of the whole sample (e.g. some samples were cut smaller to exclude artifacts or big fractures, which were obviously induced by coring and/or sample preparation).

113 Why use a primitive thresholding tool, where much more sophisticated tools for local crack detection are available (e.g. Voorn et al., 2013, 2015, Ma et al., 2020)? This is especially relevant since the entire paper hinges on the analysis of your segmented porosity.

Voorn, M., Exner, U., & Rath, A. (2013). Multiscale Hessian fracture filtering for the enhancement and segmentation of narrow fractures in 3D image data. *Computers & geosciences*, 57, 44-53.

Voorn, M., Exner, U., Barnhoorn, A., Baud, P., & Reuschlé, T. (2015). Porosity, permeability and 3D fracture network characterisation of dolomite reservoir rock samples. *Journal of Petroleum Science and Engineering*, 127, 270-285.

Ma, X., Kittikunakorn, N., Sorman, B., Xi, H., Chen, A., Marsh, M., ... & Skomski, D.

(2020). Application of Deep Learning Convolutional Neural Networks for Internal Tablet Defect Detection: High Accuracy, Throughput, and Adaptability. *Journal of Pharmaceutical Sciences*.

Response:

We are very aware of the persisting problems with crack/fracture analyses by using simple thresholding tools. However, this study does not focus on crack/fracture detection, but instead aims to exclude any cracks/fractures from the porosity analyses. In addition, pores in our samples appear as high contrast very dark grey-scale materials. In this case, the binary thresholding tool implemented by Avizo software is more than sufficient for robust porosity segmentation. Similar approaches have been previously used by multiple studies, including Menegon et al., 2015 and Gilgannon et al., 2017, where the editor is a co-author.

113 You also must have labelled the data, which degree of connectivity did you choose? This will significantly influence your pore statistics.

Response:

We assume the editor is concerned about the connectivity typically manipulated within the morphological operation "connected components" (i.e. "face" vs "edge" connectivity between voxels). We used this operation purely for visualization purposes (lines 120- 122). This limitation of the data was not implemented at all in the methodology for total porosity estimates. Thus, it does not affect our results. Nonetheless, this information is added in line 116.

"To omit the cracks, thresholded components with volumes larger than the volume of 200 face connected voxels ($439.4 \mu\text{m}^3$) were excluded from the binary label images"

119-128 This approach could be discussed considering the findings of Keller et al., 2011, 2013a (and others) on the porosity distribution in clays (as these being related to gouges).

Keller, L. M., Holzer, L., Wepf, R., & Gasser, P. (2011). 3D geometry and topology of pore pathways in Opalinus clay: Implications for mass transport. *Applied Clay Science*, 52(1-2), 85-95.

Keller, L. M., Holzer, L., Schuetz, P., & Gasser, P. (2013). Pore space relevant for gas permeability in Opalinus clay: Statistical analysis of homogeneity, percolation, and representative volume element. *Journal of Geophysical Research: Solid Earth*, 118(6), 2799-2812.

Response:

Thank you for the relevant references. Both studies are valuable contribution to the field of porosity analyses. However, they use only SEM and FIB data and do not integrate CT-data in their studies. Consequently, their approach is very different from ours and also their analyses mostly focus on pore size distribution and pore geometry. Instead, here we focus our interpretation and conclusions mainly on total porosity estimates. In our manuscript, we propose a method for total porosity calculations that in mathematically robust approach estimates total pore volumes while excluding cracks and fractures from the overall percentage. Excluding cracks from our datasets is fundamental because we are dealing with drill-hole samples that have suffered fracturing during exhumation.

121 "with limit of" is misleading, is this smaller or larger than 200 voxels?

Response:

Thank you. The text was modified to "limited up to 200 connected components"

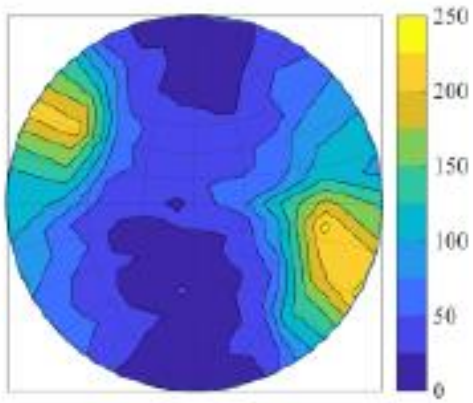
130 10 voxels as a lower limit is too small, consider the limited number of shapes you could build out of 10 cubic lego bricks - this inevitably introduces a bias in your analyses. Consider a lower limit of 5^3 voxels.

Response:

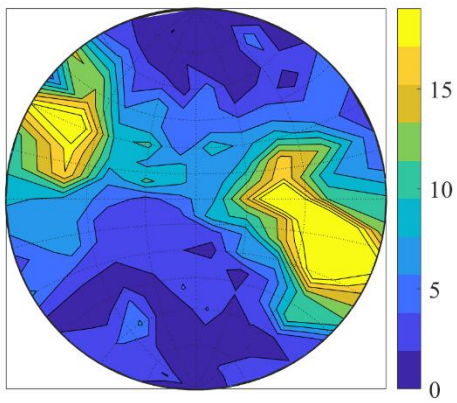
The number of shapes you can build out of 10 cubic bricks according to the sequence which defines the number of 3-dimensional polyominoes (or polycubes) with n cells is 346543, which is sufficient granularity for determining shape and orientation without bias. (N. J. A. Sloane, *A Handbook of Integer Sequences*, Academic Press, 1973)

In addition, introducing a lower limit of 5^3 voxels in our datasets (voxel size of 1.3 microns^3) will result in materials larger than $274.625 \text{ microns}^3$. Therefore, vast amount of materials of interest will be excluded. Furthermore, the shape and orientation analyses may be biased by the prevailing influence of cracks with this size.

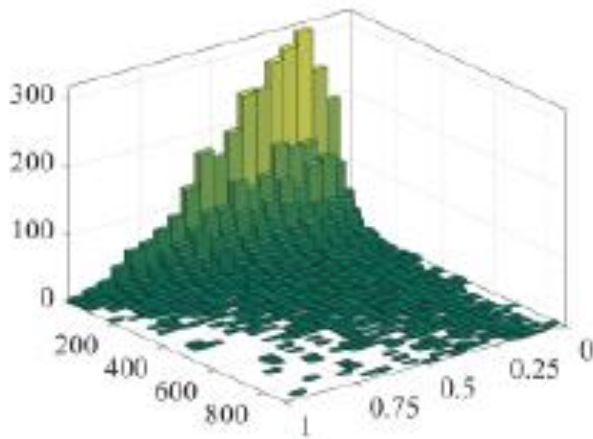
Regardless, here we present comparison between lower limits of 10 voxels and 5^3 voxels. We use as an example sample DFDP-1B 69_2.54. The figures below show that a lower limit of 5^3 (i) does not influence the pore orientation patterns; (ii) excludes vast majority of our segmented materials which are of interest, and thus introduces bias in the resulting elongation vs pore size histogram.



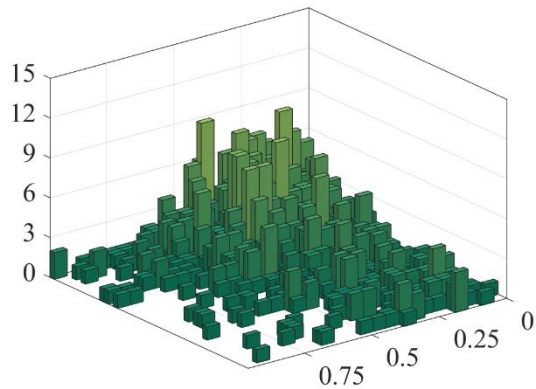
Stereonet with lower limit of 10 voxels (from figure 7)



Stereonet with lower limit of 5^3 voxels



Elongation vs pore volumes (from fig. 4) with lower limit of 10 voxels



Elongation vs pore volumes with lower limit of 5^3

135-137 I disagree with the statement that the eigenvalues describe the shape of a pore - they describe the shape of an ellipsoid, which only under fortunate circumstances will be a good approximation of the actual pore shape. To make conclusive statements on the shapes of your pores, you need to go a step further and use, e.g., Minkowski functionals (Arns et al., 2002, Lehmann et al., 2006, Wildenschild & Sheppard, 2013).

Arns, C.H., M.A. Knackstedt, and K.R. Mecke. 2002. Characterizing the morphology of disordered media. p. 37–74. K. Mecke and D.

Stoyan (ed.) In Morphology of condensed matter: Physics and geometry of spatially complex systems. Lecture Notes in Physics.

Springer, Germany.

Lehmann P et al. Tomographical imaging and mathematical description of porous media used for the prediction of fluid distribution. Vadose Zone J 2006;5(1):80.

Wildenschild, D., & Sheppard, A. P. (2013). X-ray imaging and analysis techniques for quantifying pore-scale structure and processes in subsurface porous medium systems. Advances in Water Resources, 51, 217-246.

Response:

The recommended papers deal with datasets where the porosity is connected. In these studies, shape analyses using covariance matrix decomposition would not work, thus they needed to implement other techniques. However, pores in our data are separated and the covariance matrix is calculated on each single pore. To clarify this in line 133 the text was modified to:

“Individual pores in our dataset are separated (Fig. 2c), thus the covariance matrix of each pore was calculated, and the three eigenvalues of this covariance matrix were extracted.”

Also, as we previously responded to the editor’s major comment, the covariance matrix can be calculated on any shape. Thus, our analyses are relevant, and the use of different methods would not benefit the manuscript.

155-157 The screenshot you have added in your rebuttal to J Gilgannon indicates that your segmentation captured only a very small proportion of the actual porosity. How have you chosen the threshold value for your segmentation?

Response:

We acknowledge that the image provided has a low resolution (due to Avizo software screenshot resolution) and may not show the threshold range properly. But we strongly disagree that we have not captured all the porosity in these samples. Pores were identified as the darkest grey-scale materials on images with good contrast, consequently thresholding was not challenging. We performed thresholding

by selecting the corresponding grey-scale range manually and individually for each sample due to slight brightness contrast differences in between samples. To ensure all pores were captured the selected threshold range was inspected throughout the 3D stack before thresholding being applied.

164-167 Fig 7 - what is the reference frame for these stereoplots? I see you are speculating that they trace a foliation, but obviously the maxima are all roughly at the same orientation between the plots.

Response:

In these lines we do not talk about foliation. Here, we only describe the observed maximas:

“The orientations of the individual pore units show two distinctive peaks with opposite vergence, defining bipolar distributions of pore orientations”

Later in the manuscript, we only speculate that pore orientations reflect the orientation of clay minerals. The assumption is based on the predominant distribution of pores along grain boundaries of mainly clay minerals, and the abundance of intercalary pores (lines 200-206). The similar orientation of the observed orientation maxima in all samples is due to the fact that samples were drilled parallel to the foliation. This information is added in line 104.

170 - "the gouges have composition..." - rephrase

Response: changed to “are composed of”

177 - What are the criteria by which you distinguish cracks from other types of pores in your TEM data? It is not really evident from Fig. 8.

Response:

Fracture porosity was distinguished in quartz-feldspar domains (fig. 8d) where elongated, thin void spaces are associated with multiple grains and occasionally disrupt grain boundaries. The information was added to lines 178-179.



185-187 This statement is incorrect, since this is the voxel size, which does not equate to the spatial resolution.

Response: Thank you. We now say “acquisition constrains” instead of “resolution constrains”

188-190 I think this needs to be contrasted with Keller et al (2013b)'s study on Opalinus Clay. Obviously, they investigated undeformed clay as opposed to highly sheared fault gouge, but the key finding suggests that, in clay-mineral rich portions, there may be a very substantial volume of porosity hidden. What are your arguments in support of this statement?

Keller, L. M., Schuetz, P., Erni, R., Rossell, M. D., Lucas, F., Gasser, P., & Holzer, L. (2013). Characterization of multi-scale microstructural features in Opalinus Clay. Microporous and mesoporous materials, 170, 83-94.

Response:

Thank you for this reference. We acknowledge the assumption that nano-scale porosity would not significantly influence the total porosity estimates is not robust. Thus, this statement was omitted from the manuscript.

191 (also section 3.4) How were the locations for the FIB foils chosen? How did you ensure they were representative?

Response:

The Alpine fault samples, derived during DFDP-1, have been subjected to intense microstructural analyses both onsite and post drilling operations by the DFDP-Science team. Consequently, numerous studies have described these rocks in detail (e.g. Toy et. al., 2015; Schleicher et al., 2015). Based on these previous studies and our own observations we believe we have selected areas of interest for FIB foils that yield representative results.

192-194 I don't understand how the first half of the sentence relates to the second, and how you arrive at that conclusion.

Response:

For better clarity the text has been modified, and now says:

“The pores visible on grain and phase boundaries in Figure 8b have similar sizes to the pores segmented on XCT images (> 1.3 μm in diameter), thus we conclude that this is the typical habit of both nano- and micro-pores within the Alpine Fault core (Fig. 8).”

205-208 cf. Keller et al., 2013b

Response:

We do not think that this is an appropriate reference to cite here. No change made.

209 Please restructure this section for clarity and revise paragraph structure. The reader shouldn't have to read until the end to figure out what this is about.

Response:

We have restructured the section accordingly.

213-214 How do you identify these clay minerals as authigenic?

Response:

We interpret these clays as authigenic because of the coexistence of newly precipitated fine materials and coarser grains, previously documented in detail by Schleicher et al., 2015.

214-216 Annotate these observations on the figure, and pls add references to support the pressure solution argument.

Response:

The figure is now annotated. Reference added.

228 Would be good if you provided grain size distributions for the two materials, see comment for line 98.

Response:

Grain size distribution is available as part of an unpublished PhD thesis (it is currently in final revision stage). We could include them but would then need to add the student's name to our author list. But note that substantially longer method documentation will be needed to report them here.

233 Does your analysis really demonstrate significantly different porosity values between the two cataclasite units, given the R-squared values of your regression model?

Response:

As we previously responded to the editor's second major comment, the method used here is intentionally attempting to estimate and exclude fractures within the sample data by biasing the fit which yields lower R^2 . Thus, the results presented here are robust and do demonstrate significantly different porosities. In addition, as we mention in response to reviewer James Gilgannon, similar porosity differences were also observed by calculating porosities after implementing the morphological operation "connected components".

240-251 This paragraph is a bit bold on the assumptions. First, low porosity is not necessarily consistent with low permeability, and I don't see how you verify permeability measurements? Aren't you overinterpreting a difference in porosity of 0.12%, given the uncertainties outlined in your own statistics plus the uncertainties introduced by the data processing steps and sub-sampling sites you have chosen?

Response:

We agree that porosity is not necessarily consistent with permeability and acknowledge our bad choice of wording in this paragraph. Here, we only aim to compare our porosity data with published permeability measurements on these rocks, which show similar trend. We also indicate that our porosity estimates are in agreement with previously documented permeability gradient in these rocks. The text was modified, and we now say:

"Our data thus provide independent verification is comparable with of the permeability measurements in that study (Carpenter et al., 2014) and yields increased confidence in their interpretation of a permeability gradient with distance from the PSZ"

We strongly disagree we are overinterpreting our results, because as previously described our R^2 values do not introduce uncertainties in our data (see the comment above).

254 If it is precipitation of hydrous minerals in pores (as opposed to veins), how much does the pore fluid pressure actually change as clay minerals form?

Response:

True, some of the fluids in the pores will be included in the newly formed clays. However, because these minerals also have other components (e.g. silica), the total volume of fluid involved in their formation will not be sufficient to stop a general increase in pressure as pore size reduces. We have

added a sentence 'However this pressure increase will be slightly offset by inclusion of fluids into new hydrous minerals' (in line 263)

255 Neither Byerlee nor Sibson do actually talk about precipitation in pores (but of course about fluid pressurization), could you reformulate this slightly to avoid that impression?

Response:

We modified the text to avoid misleading references. We now say:
“(i) very small decrease of these critically low total porosities due to mineral precipitation would cause fluid pressurization, which is a well-known fault weakening mechanism described by Byerlee, 1990 and Sibson, 1990” (now in line 263).

262 Is there graphite present in these samples? - It isn't highlighted in Fig 8. If not, please clarify this statement.

Response:

Graphite is not shown on the TEM images presented here. However, the presence of graphite within the Alpine Fault rocks has been previously documented and described by Kirilova et al., 2017. We modified the text to clarify this. In line 272 we now say
“which was previously documented in these rocks by previous studies (Kirilova et. al., 2017)”

Fig 2 isn't particularly helpful, since it doesn't show a workflow as such (sensu flow chart). I wonder whether 2.5D "thick slices" (see, e.g. Fig. 3 in Menegon et al., 2015, Geology) would be more better.

Response:

The aim of this figure is to show that the threshold range needed to segment all pores also captures cracks, and thus the later need to be removed for total porosity estimates and visualization purposes. Thus, the figure achieves the purposes it was designed for.

419 Fig caption "after the fractures" - "after removal of the fractures from the segmented data".

Response: The text was modified.

Fig 2c, since this is a perspective figure, the scale bar does not apply to the entirety of the image, pls consider/correct.

Response:

Thank you for this comment. We acknowledge the mistake on our side thus we removed the scale.

438/439 I don't see a difference between pores in b) and d). What are your arguments for the pores in d) being fractures?

Response:

We acknowledge that the morphology of pores in (b) and (d) may appear to the reader as fairly comparable. However, (b) represents a phyllosilicate-rich gouge area, where very elongated, extremely thin pores occur parallel to phyllosilicates orientation, thus we interpret those as “interclay porosity”. Whereas in (d) pores are in association with multiple quartz-feldspar grains and occasionally affect grain boundaries. Both interclay and fracture pores with similar characteristics were observed within San Andreas fault gauges (Janssen et al., 2011)

1 **Micro- and nano-porosity of the active Alpine Fault zone, New** 2 **Zealand**

3 Martina Kirilova^{1,2}, Virginia Toy^{1,2}, Katrina Sauer¹, François Renard^{3,4}, Klaus Gessner⁵, Richard
4 Wirth⁶, and Xianghui Xiao^{7,8}

5 ¹Institut für Geowissenschaften, Johannes Gutenberg Universität Mainz, J. J. Becher Weg 21D-55128, Mainz,
6 Germany

7
8 ~~Department of Geology, University of Otago, PO Box 56, Dunedin 9054, New Zealand~~

9 ~~²Institut für Geowissenschaften, Johannes Gutenberg Universität Mainz, J. J. Becher Weg 21D-55128, Mainz,~~
10 ~~Germany~~ Department of Geology, University of Otago, PO Box 56, Dunedin 9054, New Zealand

11 ³Department of Geosciences, The Njord Center, University of Oslo, Oslo 0316, Norway.

12 ⁴Université Grenoble Alpes, Université Savoie Mont Blanc, CNRS, IRD, IFSTTAR, ISTerre, BP53, 38041
13 Grenoble, France.

14 ~~⁵Geological Survey of Western Australia, 100 Plain Street, East Perth, WA 6004, Australia.~~ School of Earth
15 Sciences, The University of Western Australia, 35 Stirling Highway, Crawley, WA 6009

16 ⁶Helmholtz-Zentrum Potsdam, GFZ, Sektion 4.3, Telegrafenberg, 14473 Potsdam, Germany

17 ⁷Advanced Photon Source, Argonne National Laboratory, Lemont, IL 60439, USA

18 ⁸National Synchrotron Light Source II, Brookhaven National Laboratory, Upton, NY 11973, USA

19 *Correspondence to:* Martina Kirilova (martina.kirilova@uni-mainz.de)

20 **Abstract**

21 Porosity reduction in rocks from a fault core can cause ~~fluid overpressure~~ elevated pore fluid pressures, and
22 consequently influence the recurrence time of earthquakes. We investigated the porosity distribution in the New
23 Zealand's Alpine Fault core in samples recovered during the first phase of the Deep Fault Drilling Project (DFDP-
24 1B) by using two-dimensional nanoscale and three-dimensional microscale imaging. Synchrotron X-ray
25 microtomography-derived analyses of open pore spaces show total microscale porosities in the range of 0.1 to
26 0.24%. These pores have mainly non-spherical, elongated, flat shapes and show subtle bipolar orientation.
27 Transmission electron microscopy reveals that nanoscale pores ornament grain boundaries of the gouge material,
28 especially clay minerals. Our data implies that: (i) the distribution of clay minerals controls the shape and orientation
29 of the associated pores; (ii) porosity was reduced due to pressure solution processes; and (iii) mineral precipitation in
30 fluid-filled pores can affect the mechanical behaviour of the Alpine Fault by decreasing the already critically low
31 total porosity of the fault core, causing elevated pore fluid pressures ~~fluid overpressure~~, and/or introducing weak
32 mineral phases, and thus lowering the overall fault frictional strength. We conclude that the current state of porosity
33 in the Alpine Fault core is likely to play a key role in the initiation of the next fault rupture.

34 **1. Introduction**

35 Fault mechanics, fault structure and fluid flow properties of damaged fault rocks are intimately related (Gratier and
36 Gueydan, 2007; Faulkner et al., 2010). Fault rupture is associated with intense brittle fracturing that enhances
37 porosity, and thus permeability, and therefore also possible rates and directions of fluid propagation within fault
38 zones (Girault et al., 2018). Conversely, post seismic recovery mechanisms (gouge compaction and pressure
39 solution processes) result in porosity, permeability and fluid flow propagation reductions (Renard et al, 2000;
40 Faulkner et al., 2010; Sutherland et al., 2012). These processes may cause elevated pore fluid pressures within fault
41 cores, and trigger frictional failure (Sibson, 1990; Gratier et al., 2003). Therefore, the state of porosity within rocks
42 from fault cores can play a key role in fault slip.

43 The Alpine Fault of New Zealand is late in its seismic cycle (Cochran et al., 2017), so studying it allows us to
44 investigate pre-earthquake conditions that may influence earthquake nucleation and rupture processes. Recently,
45 drilling operations were undertaken in this fault zone to investigate the *in situ* conditions (Sutherland et al, 2012,
46 2017). Slug tests in the DFDP-1B borehole (Sutherland et al., 2012) and laboratory permeability measurements of
47 core samples (Carpenter et al., 2014) indicate permeability decreases by six orders of magnitude with increasing
48 proximity to the fault. Furthermore, Sutherland et al. (2012) documented a 0.53 MPa fluid pressure difference across
49 the principal slip zone (PSZ) of the fault, which suggests that the fault core has significantly lower permeability than
50 the surrounding cataclasite units. It is therefore interpreted to act as a fault seal that limits fluid circulation within its
51 hanging wall (Sutherland et al., 2012). Permeability variations like this are closely associated with the porosity
52 evolution of fault cores, and thus are likely to affect the fault strength and seismic properties (Sibson, 1990; Renard
53 et al., 2000; Gratier and Gueydan, 2007).

54 In this study, we investigate the porosity distribution in rocks from the Alpine Fault core and consider the potential
55 effects of this porosity on fault strength. We have measured open pore spaces in these rocks from X-ray computed
56 tomography (XCT) datasets and examined pore morphology by implementing quantitative shape analyses and using
57 transmission electron microscopy (TEM).

58 **2. Geological setting**

59 New Zealand's Alpine Fault (Fig. 1a) is a major active crustal-scale structure that ruptures in a large earthquake
60 every 291 ± 23 years, the last one of which occurred in 1717 (Cochran et al., 2017). The fault is the main constituent
61 of the oblique transform boundary between the Australian Plate and the Pacific Plate, accommodating around 75%
62 of the relative plate motion. Ongoing dextral strike-slip at 27 ± 5 mm yr⁻¹ along the fault has resulted in a total
63 strike-separation of ~ 480 km over the last 25 Ma (Norris and Cooper, 1995, 2001; Norris and Toy, 2014). In
64 Neogene time, a dip-slip component added to the fault motion has resulted in more than 20 km of vertical uplift of
65 the hanging wall (Norris and Cooper, 1995, 2001; Norris and Toy, 2014). Consequently, rocks comprising the
66 hanging wall of the fault have been exposed in various outcrops, where they can be studied in detail. The
67 amphibolite facies Alpine Schist is the metamorphic protolith of a ~ 1 km thick mylonite zone, which has been
68 exhumed from depth and now structurally overlies an up to 50 m thick zone of brittlely deformed cataclasites and

69 gouges (e.g. Norris and Cooper, 1995, 2001; Norris and Toy, 2014). These rocks have been investigated in outcrops
70 and from samples collected in three boreholes during the two phases of the Deep Fault Drilling Project (DFDP-1A,
71 DFDP-1B and DFDP-2B; Fig. 1a) along the Alpine Fault (Sutherland et al., 2012; Toy et al., 2015; Toy et al., 2017).

72 Most of the brittle shear displacement along the fault has been accommodated within the fault core, which includes
73 Principal Slip Zone (PSZ) gouges and cataclasite-series rocks (Toy et al., 2015). Both in surface outcrops and drill
74 core samples, the Alpine Fault manifests as a thin (5 to 20 cm thick) gouge zone with a predominantly random fabric
75 of clay-rich material (Toy et al., 2015; Schuck et al., 2020). This cohesive but uncemented layer has a significantly
76 finer grain size than the surrounding cataclasite units, which shows that the material was reworked only within this
77 layer, most probably as a result of ultracomminution due to multiple shear events under brittle conditions (Boulton
78 et al., 2012; Toy et al., 2015). The local presence of authigenic smectite clays (Schleicher et al., 2015) and calcite
79 and/or chlorite mineralization within sealed fractures and in the gouge matrix (Williams et al, 2017) indicate that
80 mineral reactions are restricted to an alteration zone within the fault core (Sutherland et al., 2012; Schuck et al.,
81 2020). The Alpine Fault core has been interpreted to have formed during a cyclical history of mineralization, shear,
82 and fragmentation (Toy et al., 2015). In addition, in the DFDP-1B borehole (Fig. 1b, Sutherland et al., 2012) fault
83 gouges occur at two distinct depths: 128.1 m (PSZ-1) and 143.85 m (PSZ-2), which shows that the slip was not
84 localized within a single gouge layer (Toy et al., 2015).

85 **3. Sample description and analytical methods**

86 **3.1 Samples**

87 Porosity analyses were performed on four samples representing PSZ gouges and cataclasites of the Alpine Fault
88 core, which were recovered from the DFDP-1B borehole (Fig. 1b, c; Sutherland et al., 2012). These are DFDP-1B
89 58_1.9, DFDP-1B 69_2.48, DFDP-1B 69_2.54 and DFDP-1B 69_2.57. Sample nomenclature includes drill core run
90 number, section number, and centimeters measured from the top of each section. These samples were recovered
91 from drilled depth of 126.94 m, 143.82 m, 143.88 m and 143.91 m, respectively.

92 Detailed lithological and microstructural descriptions of the DFDP-1B drill core were carried out simultaneously
93 with, and after the drilling operations by the DFDP-1 Science Team, and these data were later summarized by Toy et
94 al. (2015). Samples DFDP-1B 58_1.9 and DFDP-1B 69_2.48 belong to the upper foliated cataclasite units (Fig. 1b,
95 c; Toy et al., 2015). These were described as ultracataclasites with gouge-filled shears located above PSZ-1 and
96 PSZ-2 respectively. Sample DFDP-1B 69_2.54 represents the gouge layer that defines PSZ-2, whereas sample
97 DFDP-1B 69_2.57 is composed of brown ultracataclasites that belong to the lower cataclasite unit (Fig. 1b, c; Toy et
98 al., 2015).

99 **3.2 X-ray computed tomography (XCT)**

100 We imaged the samples using absorption tomography, where the signal intensity depends on how electron density
101 and bulk density attenuate a monochromatic X-ray along its path through the material (e.g. Füsseis et al. 2014). We
102 acquired the X-ray microtomography data for this study at the 2-BM beamline of the Advanced Photon Source,

103 Argonne National Laboratories USA in December 2012. The non-cylindrical samples of ~7 mm height and ~ 4 mm
104 diameter were drilled parallel to the foliation and mounted on a rotary stage and imaged with a beam energy of 20
105 keV. A charge-couple device camera collected images at 0.25° rotation steps over 180° at- sample detector distance
106 of 70 mm and FoV 2.81 mm. The voxel size was 1.3 μm. We have reconstructed the datasets with a filtered back-
107 projection parallel beam reconstruction into 32-bit gray level volumes consisting of 2083 * 2083 * 2083 voxels
108 using X-TRACT (Gureyev et al., 2011).

109 **3.3 Analyses of XCT datasets**

110 Data analyses and image processing were performed using the commercial software package Avizo 9.1 (Fig. 2).
111 Initially, the datasets were rescaled to 8-bit grey scale volumes for enhanced computer performance. In addition,
112 small volumes of interest were cropped from the whole volume before a non-local means filter was applied to
113 reduce noise (Buades et al., 2005). On the filtered gray-scale images, porosity was identified as the darkest phase
114 (Fig. 2a). The corresponding gray-scale values were thresholded, and the datasets were converted into binary form.
115 However, this threshold range also captured cracks within a sample, which are likely to result from depressurization
116 during core recovery (Fig. 2b). To omit the cracks, thresholded components with volumes larger than the volume of
117 200 face connected voxels (439.4 μm³) were excluded from the binary label images by using the morphological
118 operation ‘connected components’ built in software Avizo 9.1. Clusters of connected components were then created
119 to visualize 3D volumes of segmented pore spaces (Fig. 2c).

120 Unfortunately, this methodology results in either loss of larger pores or inclusion of small cracks depending on the
121 implemented limit of connected components, and thus calculating total porosities includes significant bias.
122 Therefore, “connected components” limited up to 200 connected voxels were used only for visualization purposes.
123 Instead, the volumes and shape characteristics of segmented materials (including cracks) were exported from Avizo
124 software in numerical format, and volume distributions within a sample were plotted on a logarithmic scale in
125 Matlab (Fig. 3). Data up to a specific volume size were fit to a polynomial curve, and then the curve was
126 extrapolated to the X intercept, which is the expected maximum pore size (Fig. 3). Total porosities were then
127 estimated by integrating the curve, which excludes all volumes on the right side of the curve. Total porosities are
128 presented as a percentage of the whole sample volume (Fig. 3). The implemented equations are presented in
129 Supplementary material 1.

130 Pore shapes were analyzed on bivariate histograms plotted on Matlab by using the numerical pore characteristics,
131 previously extracted from Avizo software. Only pore volumes between 21.97 μm³ (10 voxels) and 878.8 μm³ (400
132 voxels) were included to avoid bias in the data due to insufficient voxel count and presence of cracks, respectively.
133 Individual pores in our dataset are separated (Fig. 2c), thusFor each pore, the covariance matrix of the volumeeach
134 pore was calculated, and the three eigenvalues of this covariance matrix were extracted. These three values
135 correspond to the three main orthogonal directions in each pore (i.e. the longest, medium and shortest axes) and we
136 use them as proxies to describe pore geometry. Thus, their amplitudes provide information on the spatial extension
137 of the pore and its shape. The ratio between the medium and largest eigenvalues of each pore defines its elongation

138 (Fig. 4), the ratio between the smallest to the largest – its sphericity (Fig. 5), and the ratio of the smallest to the
139 medium – its flatness (Fig. 6).

140 The angles θ and ϕ that describe the orientation of the longest axis of each pore with respect to the main axis of the
141 3D scan were calculated. These angles were translated into trend and plunge and then plotted on a lower hemisphere
142 equal area stereographic projection with a probability density contour to display the distribution of pore unit
143 orientations (Fig. 7).

144 **3.4 Transmission electron microscopy (TEM)**

145 ~~High-resolution~~ TEM images were collected on a FEI Tecnai G2 F20 X-Twin transmission electron microscope,
146 located at the German Research Centre for Geosciences (GFZ), Potsdam, Germany (Fig. 8). The instrument is
147 equipped with field-emission gun (FEG) electron source and high-angle annular dark-field (HAADF) Detector.
148 Images were collected from samples placed on a Gatan double-tilt holder at 200kV. TEM sample preparation was
149 performed with focused ion beam (FIB) milling at GFZ Potsdam using a HELIOS system operated at 30 kV.

150 **4. Results**

151 **4.1 XCT-derived characteristics of porosity**

152 All samples contain low total porosities, ranging from 0.1% to 0.24% (Fig. 3). However, it should be noted that the
153 lower cataclasite sample (DFDP-1B 69_2.57) has twice as much pore space (Fig. 3d) as any of the other samples.
154 The characterized pore size distributions range over almost three orders of magnitude for all samples (Fig. 3).
155 Furthermore, the expected maximum pore size volume was estimated to be largest in the PSZ-2 sample (DFDP-1B
156 69_2.54), reaching $862 \mu\text{m}^3$ (Fig. 3c).

157 In all samples, shape analyses of pores with volumes between $21.97 \mu\text{m}^3$ (10 voxels) and $878.8 \mu\text{m}^3$ (400 voxels)
158 demonstrate predominantly elongated (Fig. 4), non-spherical (Fig. 5) and flat pore shapes (Fig. 6). This is
159 particularly pronounced for the smaller pore volumes. The number of elongated pores per sample is increasing in the
160 upper foliated cataclasites (Fig. 4a and b) with increasing proximity to PSZ-2, where most elongated pores occur
161 (Fig. 4c). Conversely, the lower cataclasite sample demonstrates proportionally fewer elongated pores within the
162 sample (Fig. 4d). The degree of sphericity is uniform for all samples, and pores appear as mainly non-spherical (Fig.
163 5). Few isolated spherical pores are manifested only by small pore volumes (Fig. 5). A trend of increasing the
164 number of flat pores is observed with increasing sample depth (Fig. 6), and most flat pores are detected in the lower
165 cataclasite (Fig. 6d).

166 The orientations of the individual pore units show two distinctive peaks with opposite vergence, defining bipolar
167 distributions of pore orientations (Fig. 7). The observed bipolarity is subtle in samples DFDP-1B 58_1.9 (Fig. 7a)
168 and DFDP-1B 69_2.48 (Fig. 7b), and more obvious in samples DFDP-1B 69_2.54 (Fig. 7c) and DFDP-1B 69_2.57
169 (Fig. 7d).

170 **4.2 Microstructural characteristics of porosity**

171 TEM characterization of the gouge material from PSZ-2 (sample DFDP-1B 69_2.54) reveals that the Alpine Fault
172 gouges ~~have composition, are composed of comprising~~ angular quartz and/or feldspar fragments (~200 nm in size),
173 wrapped by smaller phyllosilicates (< 100 nm long). This random fabric is ornamented by nanoscale pores (< 50
174 nm), distributed along all grain and phase boundaries, especially abundant along clay minerals (Fig. 8a).

175 The gouge material also demonstrates phyllosilicate-rich areas, defined by an increase in the clay/clast ratio. In these
176 zones, fine (< 100 nm long) and coarser (few μm long) clay grains coexist and are aligned in wavy fabric that
177 surrounds sporadic protolith fragments (Fig. 8b). Pore spaces are again distributed along the boundaries of the
178 constituent mineral grains but some of them are larger (~0.5 μm) ~~with and thin~~ ellipsoidal or elongated shapes (Fig.
179 8b, c). These pores are commonly associated with inter-clay layer porosity. Large size pores are also observed along
180 quartz-feldspar grains, where pores are associated with multiple grains and occasionally disrupt grain boundaries,
181 thus were labelled as cracks along boundaries of quartz and/or feldspar grains (i.e. fracture porosity; (Fig. 8d).

182 **5. Discussion**

183 **5.1 Characteristics of porosity within the Alpine Fault core**

184 Porosity analyses of samples from, or in close proximity to the two PSZs encountered in the DFDP-1B drill core
185 reveal total pore volumes between ~ 0.1 and 0.24% (Fig. 3). These values are significantly lower than the porosity
186 estimates from other active faults in the world, such as: 0.2 to 5.7% total porosity in the core of the Nojima Fault,
187 Japan (Surma et al., 2003) and 0 to 18% in the San Andreas Fault core (Blackburn et al., 2009). The Alpine Fault
188 core contains total pore space volumes, comparable only with the lower porosities in these previous studies. It
189 should be noted that the smallest pore spaces captured in the XCT datasets are 1.3 μm in size due to resolution
190 acquisition constrains, whereas nanoscale porosity was identified on the TEM images. Therefore, the estimated total
191 porosities represent only minimum values of the open pore spaces in the Alpine Fault core. ~~However, the addition of~~
192 ~~nanoscale porosity volumes is unlikely to dramatically affect the final total porosity of these rocks because they~~
193 ~~comprise a very small total volume.~~

194 TEM images presented here mainly focus on nano-scale materials (Fig. 8a, c, d) but were also used to describe the
195 distribution of micro-porosity in these rocks (Figure 8b). The pores visible on grain and phase boundaries in
196 figure 8b pores have similar sizes comparable to the small range of pores segmented on XCT images (> 1.3 μm in
197 diameter), and thus we conclude that this is the typical habit of both nano- and micro-pores within the Alpine Fault
198 core are distributed on grain and phase boundaries, especially of clay minerals (Fig. 8). In addition, both quantitative
199 micro-porosity shape analyses (Fig. 4, 5 and 6) and nano-pores identified on TEM images (Fig. 8) reveal that a
200 significant population of pores are predominantly non-spherical with elongated, flat shapes. We attribute this
201 observation to the tendency of these pores to ornament clay minerals where pores are attained and elongated along
202 their (001) planes (Fig. 8b, c and d).

203 Foliation in the upper cataclasites is defined by clay-sized phyllosilicates, that become more abundant with
204 proximity to the PSZ (Toy et al., 2015), where weak clay fabric is developed (Schleicher et al., 2015). This gradual
205 enrichment in clay minerals coincides with the subtle development of bipolar distributions of pore orientations with
206 increasing sample depth (Fig. 7). This observation and the fact that pores are mainly attained along grain boundaries
207 of clays (Fig. 8) suggest that the distribution of clay minerals also controls pore orientations within the Alpine Fault
208 core. Previously, the phyllosilicate foliation in the Alpine Fault cataclasites has been used to define shear direction
209 (Toy et al., 2015). Thus, we speculate that pore orientations in these rocks are also systematically related to the
210 kinematic framework of the shear zone. If these pores represent remnants of fluid channels, their spatial orientation
211 is likely to reflect the fluid flow directions during deformation. To address this possibility more data for systematic
212 analyses of pore orientations are needed.

213 **5.2 Porosity reduction within the Alpine Fault core**

214 The comparatively lower porosity estimates of the Alpine Fault core than other active faults (e.g. the Nojima Fault,
215 Surma et al., 2003, and the San Andreas Fault, Blackburn et al., 2009) can be attributed to the fact that the Alpine
216 Fault is late in its seismic cycle and the last seismic event occurred in 1717 (Cochran et al., 2017). Porosity of the
217 fault core is considered to evolve during the seismic cycle when fault rupture can cause porosity increase up to 10%
218 (Marone et al., 1990), and the consequent healing mechanisms lead to porosity decrease over time due to mechanical
219 compaction of the fault gouge and/or elimination of pore spaces within the fault core due to pressure solution
220 processes (Sibson, 1990; Renard et al., 2000; Faulkner et al., 2010). TEM data presented here show abundance of
221 newly precipitated authigenic clays, wrapped around coarser clay minerals (Fig. 8b). Furthermore, delicate clay
222 minerals form fringe structures (Fig. 8a), and strain shadows (Fig. 8c) around larger quartz-feldspar grains. These
223 microstructural observations demonstrate that pressure solution processes operated within these rocks (Toy et al.,
224 2015).

225 Evidence for pressure solution processes has been previously documented in all units, comprising the Alpine Fault
226 core (Toy et al., 2015). Abundant precipitation of alteration minerals (Sutherland et al., 2012), calcite filled
227 intragranular and cross-cutting veins (Williams et al., 2017), and the occurrence of newly formed smectite clays
228 (Schleicher et al., 2015) indicate extensive fluid-rock reactions. In addition, anastomosing networks of opaque
229 minerals (such as graphite; Kirilova et al., 2017), which define foliation in the upper cataclasites (Toy et al., 2015),
230 have been interpreted to be concentrated by pressure solution processes during aseismic creep (Toy et al., 2015;
231 Gratier et al., 2011). The petrological characteristics of the Alpine Fault core lithologies identify solution transfer
232 mechanisms likely were the dominant mechanism for pore closure within these rocks.

233 Post-rupture porosity reduction is known to operate three to four times faster within fine-grained fault gouges than in
234 coarser-grained cataclasites (Walder and Nur, 1984; Sleep and Blanpied, 1992; Renard et al., 2000), which may
235 explain the differences in total porosity between the gouge-containing samples and the footwall ultracataclasite –
236 DFDP-1B 69-2.57 (Fig. 3). Furthermore, previous studies documented less carbonate and phyllosilicate filling of
237 cracks in the Alpine Fault footwall cataclasites as compared to the hanging wall cataclasites (Sutherland et al., 2012;

238 Toy et al., 2015), suggesting more reactive fluids are present and isolated within the hanging wall of the Alpine
239 Fault. Thus, more intense dissolution-precipitation processes took place in the fault's hanging wall, which very
240 likely resulted in more efficient porosity reduction, as demonstrated by our porosity estimates (Fig. 3).

241 ~~As aforementioned, porosity reduction is known to increase with time after an earthquake event due to post-rupture~~
242 ~~healing mechanisms (Sibson, 1990; Renard et al., 2000; Faulkner et al., 2010). Thus, the comparatively lower~~
243 ~~porosity estimates of the Alpine Fault core than other active faults (e.g. the Nojima Fault, Surma et al., 2003, and the~~
244 ~~San Andreas Fault, Blackburn et al., 2009) can be attributed to the fact that the Alpine Fault is late in its seismic~~
245 ~~cycle (Cochran et al., 2017).~~

246 5.3 Effects of porosity on the Alpine Fault strength

247 The extremely low porosity estimates presented here (Fig. 3) are consistent with the low permeabilities of 10^{-18} m²
248 measured experimentally in clay-rich cataclasites and gouges from the Alpine Fault zone (Carpenter et al., 2014). In
249 addition, the documented difference of total porosities between the hanging wall and footwall samples (Fig. 3)
250 implies different intensity of pressure solution processes, and thus compartmented fluid propagation. Our data ~~thus~~
251 ~~provide independent verification is comparable with~~ of the permeability measurements in that study (Carpenter et
252 al., 2014) and yields increased confidence in their interpretation of a permeability gradient with distance from the
253 PSZ, which itself acts as a hydraulic seal (Sutherland, et al., 2012). The existence of such a barrier to flow is
254 characteristic for faults undergoing creep and locked faults (Rice, 1992; Labaume et al., 1997; Wiersberg and
255 Erzinger, 2008). However, much higher permeabilities in the surrounding damaged rocks (Carpenter et al., 2014)
256 allow fast propagation of fluids within them and can cause localization of high fluid pressures on one side or the
257 other of a hydraulic seal (Sibson, 1990). Such fluid pressures can enhance gouge compaction and pressure solution
258 processes within the fault core, which will eventually introduce zones of weakness and thus may trigger fault slip
259 (Faulkner et al., 2010).

260 Previous studies and the observations presented here show that fluids were present in the Alpine Fault rocks. Fluid-
261 filled pores represent a favorable environment for mineral precipitation, which can affect the fault strength in two
262 ways: (i) Very small decrease of these critically low total porosities due to mineral precipitation would cause fluid
263 pressurization, which is a well-known fault weakening mechanism ~~described by (Byerlee, 1990; and Sibson, 1990).~~
264 ~~However, this pressure increase will be slightly offset by inclusion of fluids into new hydrous minerals;~~ (ii)
265 deposition of frictionally weak phases (such as clay minerals and graphite), especially if they decorate grain contacts
266 and/or form interlinked weak layers, would lower the overall frictional strength (Rutter et al., 1976; Niemeijer et al.,
267 2010).

268 Precipitation of authigenic clay minerals was identified on our TEM data (Fig. 8) and also documented by previous
269 studies (Schleicher et al., 2015). As well as having low frictional strengths (Moore and Lockner, 2004), clay
270 minerals may also contribute to the formation of an impermeable seal if they form an aligned fabric, and thus can
271 enhance the likelihood of fluid-pressurization in the fault rocks (Rice, 1992; Faulkner et al., 2010). In addition,
272 graphite, which was previously documented in these rocks by previous studies (Kirilova et al., 2017), may

273 effectively weaken the fault due to mechanical smearing (Rutter et al., 2013) and/or localized precipitation within
274 strained areas (Upton and Craw, 2008). Such graphite precipitation within shear surfaces was previously
275 documented by Kirilova et al. (2017).

276 In summary, the presence of trapped fluids in the low porosity rocks of the Alpine Fault core possibly controls the
277 mechanical behavior of the fault and could be responsible for future rupture initiation due to fluid pressurization
278 and/or precipitation of weak mineral phases. This hypothesis is further supported by an experimental study showing
279 that the DFDP-1 gouges are frictionally strong in the absence of elevated fluid pressure (Boulton et al., 2014).

280 **6. Conclusions**

281 Analyses of XCT-datasets and TEM images of borehole samples from the core of the Alpine Fault reveal micro- and
282 nanoscale pores, distributed along grain boundaries of the constituent mineral phases, especially clay minerals. The
283 tendency of these pores to ornament clays defines their predominantly non-spherical, elongated, flat shapes and the
284 bipolar distribution of pore orientations. The documented extremely low total porosities (from 0.1 to 0.24 %) in
285 these rocks suggest effective porosity reduction. Microstructural observations presented here and documented in
286 previous studies indicate that pressure solution processes were the dominant healing mechanism, and that fluids
287 were present in these rocks. Therefore, fluid-filled pores may be places where ~~fluid-overpressures~~elevated pore fluid
288 pressures develop, due to further mineral precipitation that decreases the already critically low total porosities.
289 Alternatively, they may also facilitate deposition of weak mineral phases (such as clay minerals and graphite) that
290 may very effectively weaken the fault. We conclude that the current state of the fault core porosity is possibly a
291 controlling factor on the mechanical behaviour of the Alpine Fault and will likely play a key role in the initiation of
292 the next fault rupture.

293 **Data availability.**

294 Matlab code and numerical data of pore volumes can be found in Supplementary material 1.

295 **Authors contribution**

296 Kirilova reconstructed, processed, and analysed the XCT datasets presented here, interpreted the TEM data and
297 prepared the manuscript. Most of this work was performed during Kirilova's PhD under the academic guidance of
298 Toy. Toy and Gessner collected the XCT data with technical support by Xiao. Renard and Sauer contributed with
299 valuable discussion about XCT data analyses. Wirth enabled TEM data acquisition and provided his expertise on
300 TEM data interpretation. The final version of this manuscript benefits from collective intellectual input.

301 **Competing interests**

302 The authors declare that they have no conflict of interest.

303 **Acknowledgments**

304 We gratefully acknowledge funding from the Advances Photon Source (GUP 31177). This research used resources
305 of the Advanced Photon Source, a U.S. Department of Energy (DOE) Office of Science User Facility operated for
306 the DOE Office of Science by Argonne National Laboratory under Contract No. DE-AC02-06CH11357. Avizo
307 workstation was built at the University of Otago with financial support provided by Nvidia, Corporation Royal
308 Society of New Zealand's Rutherford fellowships (16-UOO-001), the Ministry of Business and Innovation's
309 Endeavor Fund (C05X1605/GNS-MBIE00056), and a subcontract to the Tectonics and Structure of Zealandia
310 Program at GNS Science (GNS-DCF00020). Publishing bursary funding provided by the University of Otago is
311 greatly appreciated. We thank Sherry Mayo for helping with the reconstruction process of XCT data and Andrew
312 Squelch for providing use of the Avizo workstation, located at CSIRO, Perth, Australia during the initial data
313 analyses. Special thanks to Reed Debaets for assistance with the development of Matlab code. [Klaus Gessner](#)
314 [publishes with permission of the Executive Director, Geological Survey of Western Australia.](#)

315 **References**

316 Berryman, K. R., Cochran, U. A., Clark, K. J., Biasi, G. P., Langridge, R. M., and Villamor, P., 2012, Major
317 earthquakes occur regularly on an isolated plate boundary fault, *Science*, 336(6089), 1690-1693.

318 Blackburn, E. D., Hadizadeh, J., and Babaie, H. A., 2009, A microstructural study of SAFOD gouge from actively
319 creeping San Andreas Fault zone: Implications for shear localization models, *in* AGU Fall Meeting Abstracts.

320 Buades, A., Coll, B. and Morel, J. M., 2005, A non-local algorithm for image denoising, *in* Computer Vision and
321 Pattern Recognition, IEEE Computer Society Conference, Vol. 2, pp. 60-65.

322 Boulton, C., Carpenter, B. M., Toy, V., and Marone, C., 2012, Physical properties of surface outcrop cataclastic
323 fault rocks, Alpine Fault, New Zealand, *Geochemistry, Geophysics, Geosystems*, 13, Q01018,
324 doi:10.1029/2011GC003872.

325 Boulton, C., Moore, D. E., Lockner, D. A., Toy, V. G., Townend, J., and Sutherland, R., 2014, Frictional properties
326 of exhumed fault gouges in DFDP-1 cores, Alpine Fault, New Zealand, *Geophysical Research Letters*, 41(2), 356-
327 362.

328 Byerlee, J., 1990, Friction, overpressure and fault normal compression, *Geophysical Research Letters*, 17(12), 2109-
329 2112.

330 Carpenter, B. M., Kitajima, H., Sutherland, R., Townend, J., Toy, V. G., and Saffer, D. M., 2014, Hydraulic and
331 acoustic properties of the active Alpine Fault, New Zealand: Laboratory measurements on DFDP-1 drill core, *Earth*
332 *and Planetary Science Letters*, 390, 45-51.

333 Cochran, U. A., Clark, K. J., Howarth, J. D., Biasi, G. P., Langridge, R. M., Villamor, P., ... and Vandergoes, M. J.,
334 2017, A plate boundary earthquake record from a wetland adjacent to the Alpine fault in New Zealand refines
335 hazard estimates, *Earth and Planetary Science Letters*, 464, 175-188.

336 Faulkner, D. R., Jackson, C. A. L., Lunn, R. J., Schlische, R. W., Shipton, Z. K., Wibberley, C. A. J., and Withjack,
337 M. O., 2010, A review of recent developments concerning the structure, mechanics and fluid flow properties of fault
338 zones, *Journal of Structural Geology*, 32(11), 1557-1575.

339 Fussesis, F., Xiao, X., Schrank, C., and De Carlo, F., 2014, A brief guide to synchrotron radiation-based
340 microtomography in (structural) geology and rock mechanics, *Journal of Structural Geology*, 65, 1-16.

341 Girault, F., Adhikari, L. B., France-Lanord, C., Agrinier, P., Koirala, B. P., Bhattarai, M., and Perrier, F., 2018,
342 Persistent CO₂ emissions and hydrothermal unrest following the 2015 earthquake in Nepal, *Nature*
343 *Communications*, 9(1), 2956.

344 Gratier, J.-P., Favreau, P., and Renard, F., 2003, Modelling fluid transfer along California faults when integrating
345 pressure solution crack sealing and compaction processes, *Journal of Geophysical Research*, 108, 2104,
346 doi:10.1029/2001JB000380, B2.

347 Gratier, J. P., 2011, Fault permeability and strength evolution related to fracturing and healing episodic processes
348 (years to millennia): the role of pressure solution, *Oil and Gas Science and Technology—Revue d'IFP Energies*
349 *nouvelles*, 66(3), 491-506.

350 Gratier, J. P., and Gueydan, F., 2007, Effect of Fracturing and Fluid–Rock Interaction on Seismic Cycles, *Tectonic*
351 *Faults: Agents of Change on a Dynamic Earth*, 95, 319e356.

352 Gureyev, TE, Nesterets, Y, Ternovski, D, Wilkins, SW, Stevenson, AW, Sakellariou, A and Taylor, JA 2011,
353 Toolbox for advanced x-ray image processing, in *Advances in Computational Methods for X-Ray Optics II* edited
354 by M Sanchez del Rio and O Chubar, *Advances in Computational Methods for X-Ray Optics II*, San Diego, USA,
355 21-25 August 2011: SPIE - The International Society of Optics and Photonics 8141.

356 Janssen, C., Wirth, R., Reinicke, A., Rybacki, E., Naumann, R., Wenk, H. R., and Dresen, G., 2011, Nanoscale
357 porosity in SAFOD core samples (San Andreas Fault), *Earth and Planetary Science Letters*, 301(1), 179-189.

358 Labaume, P., Maltman, A. J., Bolton, A., Tessier, D., Ogawa, Y., and Takizawa, S. 1997, Scaly fabrics in sheared
359 clays from the décollement zone of the Barbados accretionary prism, *in* Shipley, T.H., Ogawa, Y., Blum, P., and
360 Bahr, J.M. (Eds.), *Proceedings of the Ocean Drilling Program Scientific Results*, 59-78.

361 Kirilova, M., Toy, V. G., Timms, N., Halfpenny, A., Menzies, C., Craw, D., ... and Carpenter, B. M., 2017, Textural
362 changes of graphitic carbon by tectonic and hydrothermal processes in an active plate boundary fault zone, Alpine
363 Fault, New Zealand, Geological Society, London, Special Publications, 453, SP453-13.

364 Marone, C., Raleigh, C. B., and Scholz, C. H., 1990, Frictional behavior and constitutive modeling of simulated
365 fault gouge, *Journal of Geophysical Research: Solid Earth*, 95(B5), 7007-7025.

366 Niemeijer, A., Marone, C., and Elsworth, D., 2010, Fabric induced weakness of tectonic faults, *Geophysical*
367 *Research Letters*, 37, L03304, doi:10.1029/2009GL041689.

368 Norris, R. J., and Cooper, A. F., 1995, Origin of small-scale segmentation and transpressional thrusting along the
369 Alpine fault, New Zealand. *Geological Society of America Bulletin*, 107(2), 231-240.

370 Norris, R. J., and Cooper, A. F., 2001, Late Quaternary slip rates and slip partitioning on the Alpine Fault, New
371 Zealand. *Journal of Structural Geology*, 23(2), 507-520.

372 Norris, R. J., and Toy, V. G., 2014, Continental transforms: A view from the Alpine Fault, *Journal of Structural*
373 *Geology*, 64, 3-31.

374 Renard, F., Gratier, J. P., and Jamtveit, B., 2000, Kinetics of crack-sealing, intergranular pressure solution, and
375 compaction around active faults, *Journal of Structural Geology*, 22(10), 1395-1407.

376 Rice, J. R., 1992, Fault stress states, pore pressure distributions, and the weakness of the San Andreas fault,
377 *International Geophysics*, 51, 475-503.

378 Rutter, E. H., and Elliott, D., 1976, The kinetics of rock deformation by pressure solution, *Philosophical*
379 *Transactions for the Royal Society of London, Series A, Mathematical and Physical Sciences*, 283, 203-219.

380 Rutter, E. H., Hackston, A. J., Yeatman, E., Brodie, K. H., Mecklenburgh, J., and May, S. E., 2013, Reduction of
381 friction on geological faults by weak-phase smearing, *Journal of Structural Geology*, 51, 52-60.

382 Schleicher, A. M., Sutherland, R., Townend, J., Toy, V. G., and Van Der Pluijm, B. A., 2015, Clay mineral
383 formation and fabric development in the DFDP-1B borehole, central Alpine Fault, New Zealand, *New Zealand*
384 *Journal of Geology and Geophysics*, 58(1), 13-21.

385 Schuck, B., Schleicher, A. M., Janssen, C., Toy, V. G., and Dresen, G., 2020, Fault zone architecture of a large
386 plate-bounding strike-slip fault: a case study from the Alpine Fault, New Zealand. *Solid Earth*, 11(1), 95-124.

387 Secor, D. T., 1965, Role of fluid pressure in jointing, *American Journal of Science*, 263(8), 633-646.

388 Sibson, R. H., 1990, Conditions for fault-valve behaviour, Geological Society, London, Special Publications, 54(1),
389 15-28.

390 Sleep, N. H., and Blanpied, M. L., 1992, Creep, compaction and the weak rheology of major faults, Nature,
391 359(6397), 687-692.

392 Surma, F., Géraud, Y., and Pezard, P., 2003, Porosity network of the Nojima fault zone in the Hirabayashi hole
393 (Japan), *in* EGS-AGU-EUG Joint Assembly.

394 Sutherland, R., Eberhart-Phillips, D., Harris, R. A., Stern, T., Beavan, J., Ellis, S Henrys, S., Cox, S., Norris, R.J.,
395 Berryman, K.R. and Townend, J., 2007, Do great earthquakes occur on the Alpine fault in central South Island, New
396 Zealand?, In: A continental plate boundary: tectonics at South Island, New Zealand, Geophysical Monograph,
397 American Geophysical Union, 235-251.

398 Sutherland, R., Toy, V. G., Townend, J., Cox, S. C., Eccles, J. D., Faulkner, D. R Prior, D.J., Norris, R.J., Mariani,
399 E., Boulton, C. and Carpenter, B.M., 2012, Drilling reveals fluid control on architecture and rupture of the Alpine
400 fault, New Zealand, *Geology*, 40(12), 1143-1146.

401 Sutherland, R., Townend, J., Toy, V., Upton, P., Coussens, J., Allen, M., and Boles, A., 2017, Extreme
402 hydrothermal conditions at an active plate-bounding fault, *Nature*, 546, 137-140, doi: 10.1038/nature22355.

403 Toy, V. G., Boulton, C. J., Sutherland, R., Townend, J., Norris, R. J., Little, T. A., and Scott, H., 2015, Fault rock
404 lithologies and architecture of the central Alpine fault, New Zealand, revealed by DFDP-1 drilling, *Lithosphere*,
405 L395-1.

406 Toy, V. G., Sutherland, R., Townend, J., Allen, M., Becroft, L., Boles, A., Boulton., C., Carpenter, B., Cooper, A.,
407 Cox, S., Daube, C., Faulkner., D., Halfpenny, A., Kato, N., Keys, S., Kirilova, M., Kometani, Y., Little, T., Mariani,
408 E., Melosh, B., Menzies, C., Morales, L., Morgan, C., Mori, C., Niemeijer, A., ... and Zimmer, M., 2017, Bedrock
409 Geology of DFDP-2B, Central Alpine Fault, New Zealand, *New Zealand Journal of Geology and Geophysics.*,
410 60(4), 497-518.

411 Upton P. and Craw D., 2008, Modelling the role of graphite in development of a mineralised mid-crustal shear zone,
412 Macraes mine, New Zealand, *Earth and Planetary Science Letters* 266: 245-255.

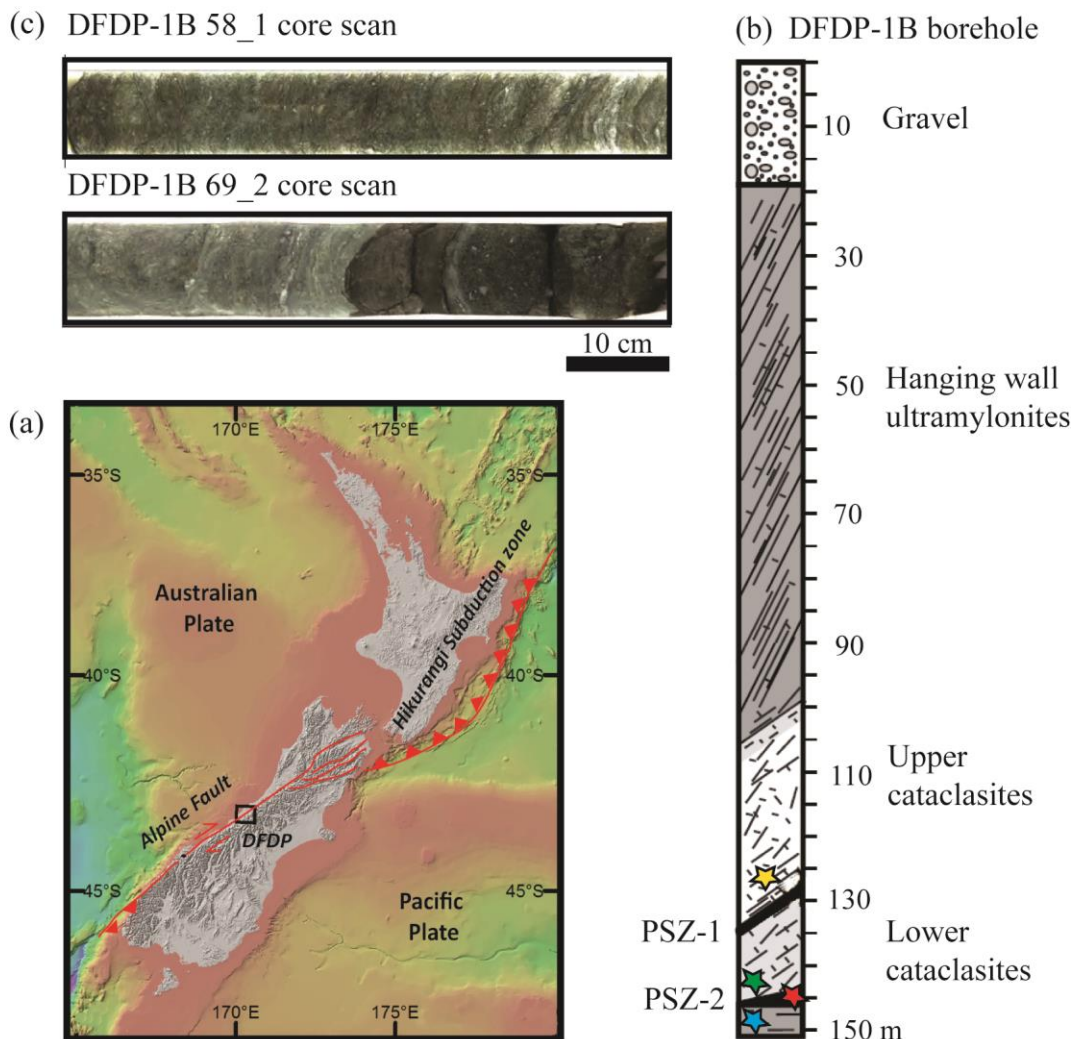
413 Walder, J., and Nur, A., 1984, Porosity reduction and crustal pore pressure development, *Journal of Geophysical*
414 *Research: Solid Earth*, 89(B13), 11539-11548.

415 Walsh, J. B., 1965, The effect of cracks on the uniaxial elastic compression of rocks, *Journal of Geophysical*
416 *Research*, 70(2), 399-411.

417 Wiersberg, T and Erzinger, J 2008, Origin and spatial distribution of gas at seismogenic depths of the San Andreas
418 Fault from drill-mud gas analysis: Applied Geochemistry, v. 23, no. 6, p. 1675-1690.

419 Williams, J. N., Toy, V. G., Smith, S. A and Boulton, C., 2017, Fracturing, fluid-rock interaction and mineralisation
420 during the seismic cycle along the Alpine Fault, Journal of Structural Geology, 103, 151-166.

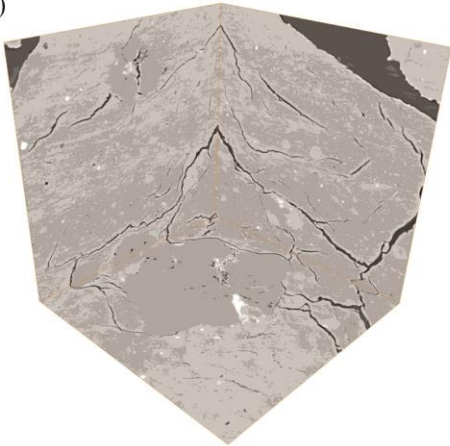
421 **Figures**



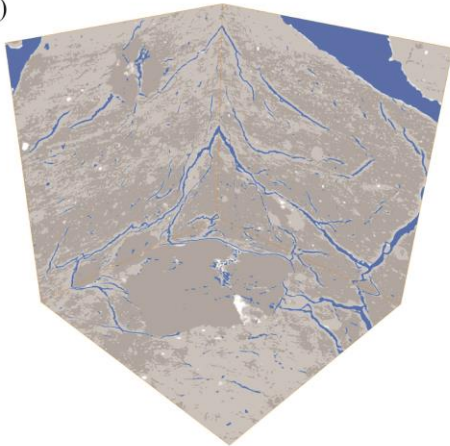
422
423 **Figure 1.** (a) Location map of DFDP drill sites (a bathymetric map compiled by NIWA). Drill site coordinates:
424 43°17'5"S, 170°24'22"E (b) Schematic diagram of the sampled lithologies in DFDP-1B borehole (modified after
425 Sutherland et al., 2012). (c) Scans of DFDP-1B drill core. Samples were collected from the locations indicated with
426 stars: yellow – DFDP-1B 58_1.9; green – DFDP-1B 69_2.48; red – DFDP-1B 69_2.54; blue – DFDP-1B 69_2.57.

DFDP - 1B 69-2.57

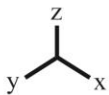
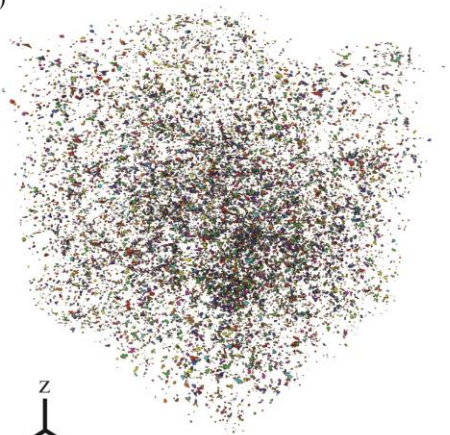
(a)



(b)



(c)



427

428

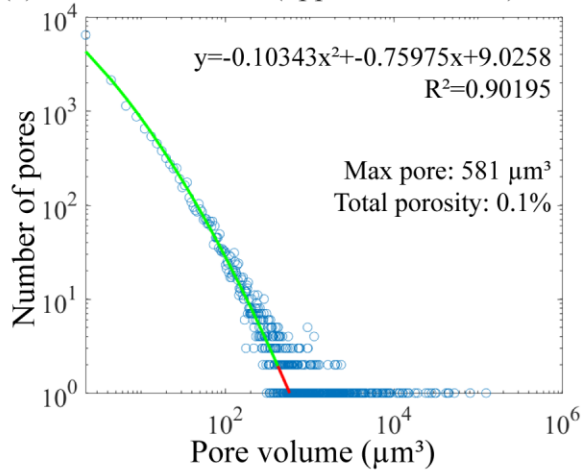
429

430

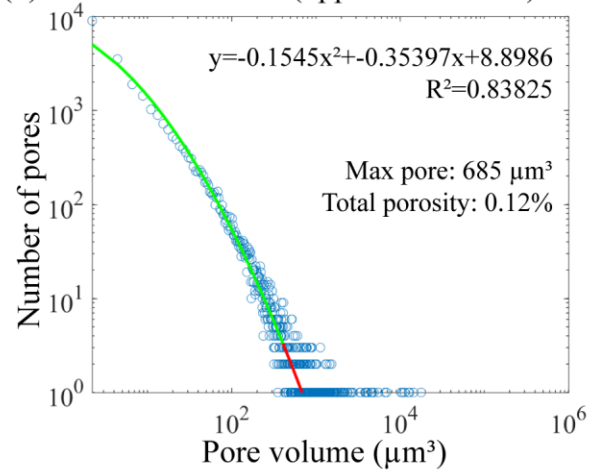
431

Figure 2. X-ray tomography data processing workflow. (a) Gray scale images in xy, xz and yz directions (b) Threshold of the darkest gray scale phase in each sample, corresponding to voids (pores and fractures); (c) 3D volume of the segmented pore spaces after removal of the fractures due to sample decompaction and coring damaging effects were removed.

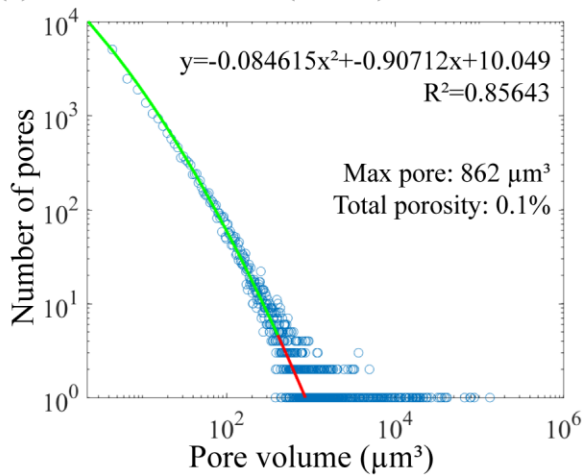
(a) DFDP-1B 58-1.9 (upper foliated ccl)



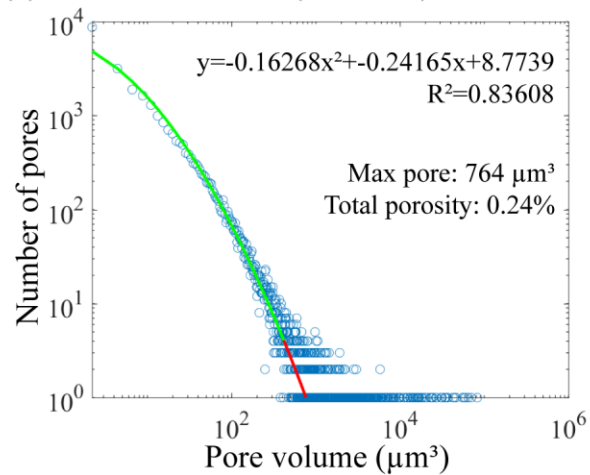
(b) DFDP-1B 69-2.48 (upper foliated ccl)



(c) DFDP-1B 69-2.54 (PSZ-2)



(d) DFDP-1B 69-2.57 (lower ccl)



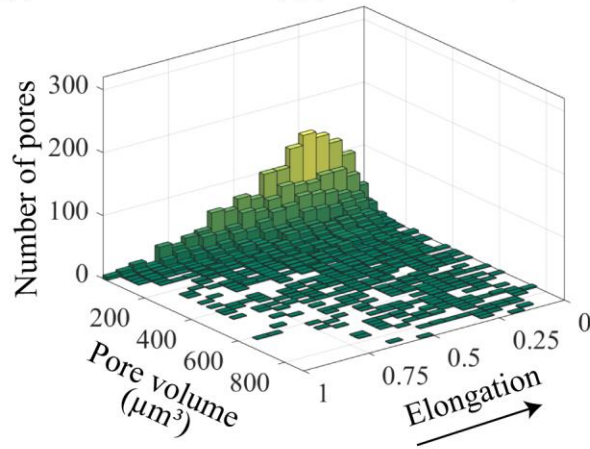
432

433

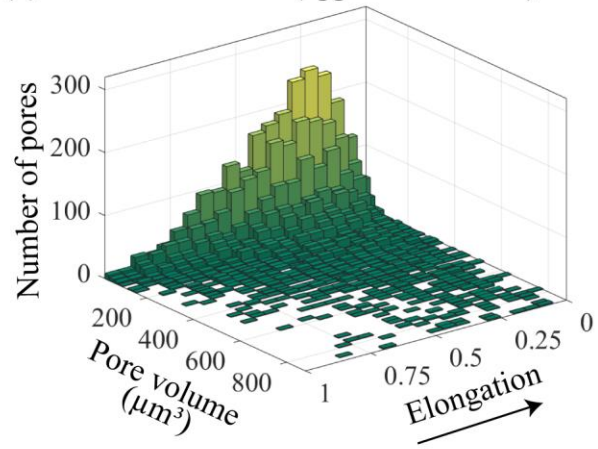
434

Figure 3. Plots of pore volume versus number of pores for each sample. Estimates of total porosity and size of the maximum expected pore are also shown, as well as the curve fitting function for each dataset.

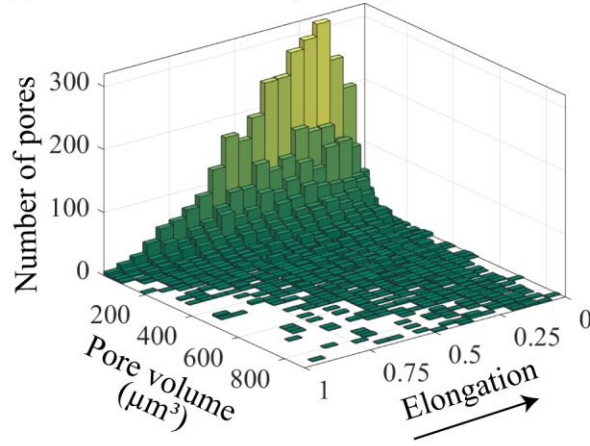
(a) DFDP-1B 58-1.9 (upper foliated ccl)



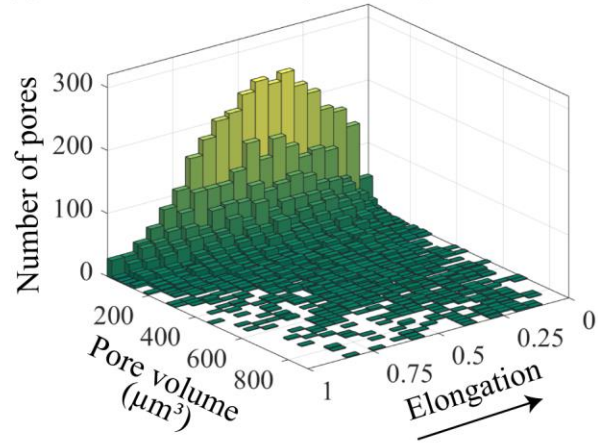
(b) DFDP-1B 69-2.48 (upper foliated ccl)



(c) DFDP-1B 69-2.54 (PSZ-2)



(d) DFDP-1B 69-2.57 (lower ccl)

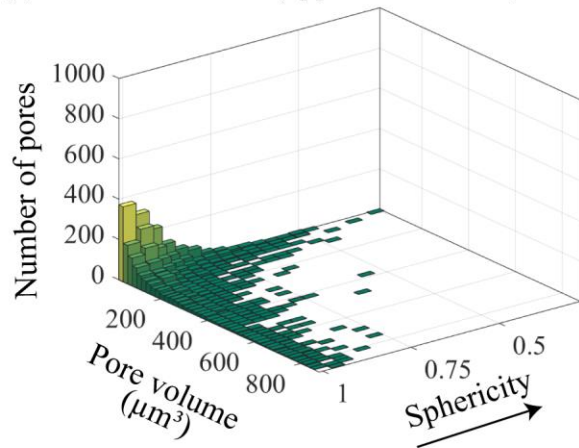


435

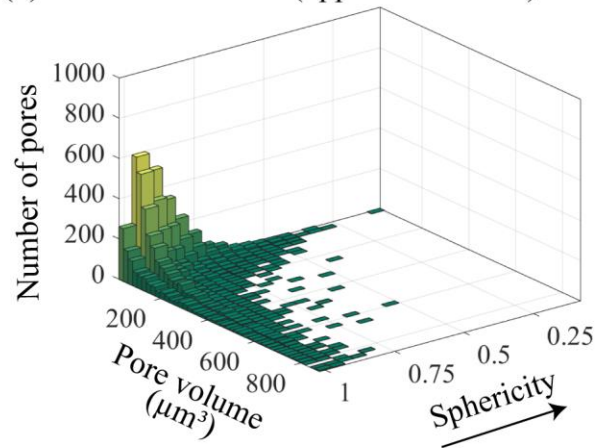
436 **Figure 4.** Bivariate histograms showing elongation versus pore volume (μm^3) and number of pores for each sample.

437 The arrow indicates the direction of increasing elongation.

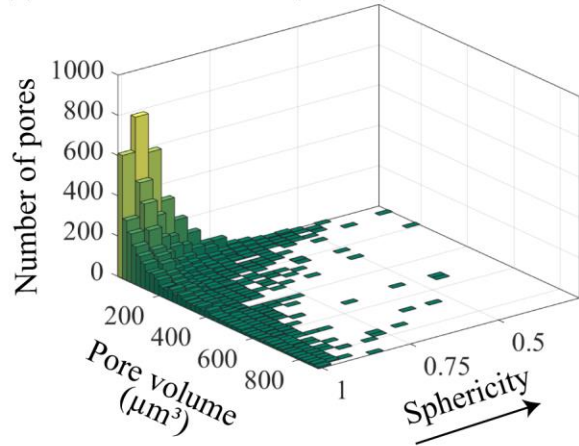
(a) DFDP-1B 58-1.9 (upper foliated ccl)



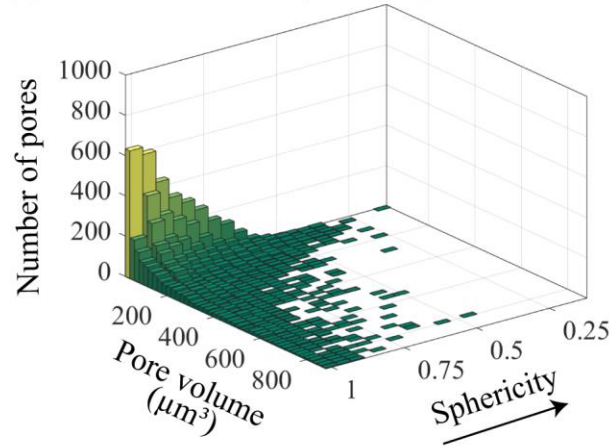
(b) DFDP-1B 69-2.48 (upper foliated ccl)



(c) DFDP-1B 69-2.54 (PSZ-2)



(d) DFDP-1B 69-2.57 (lower ccl)

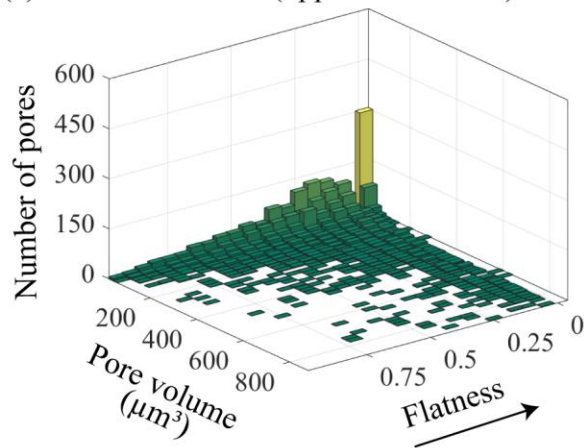


438

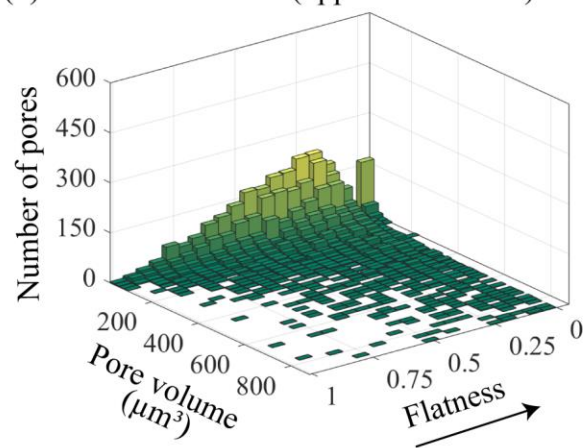
439 **Figure 5.** Bivariate histograms showing sphericity versus pore volume (μm^3) and number of pores for each sample.

440 The arrow indicates the direction of increasing sphericity.

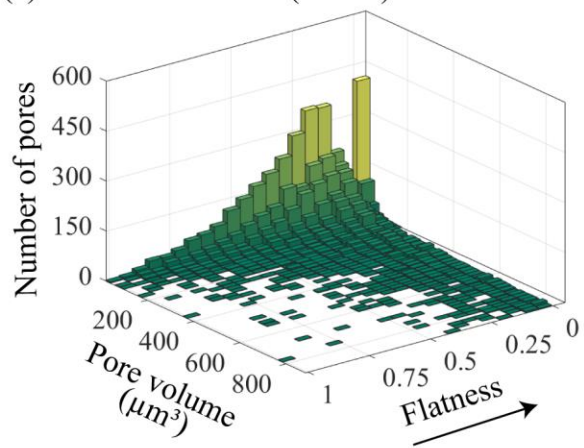
(a) DFDP-1B 58-1.9 (upper foliated ccl)



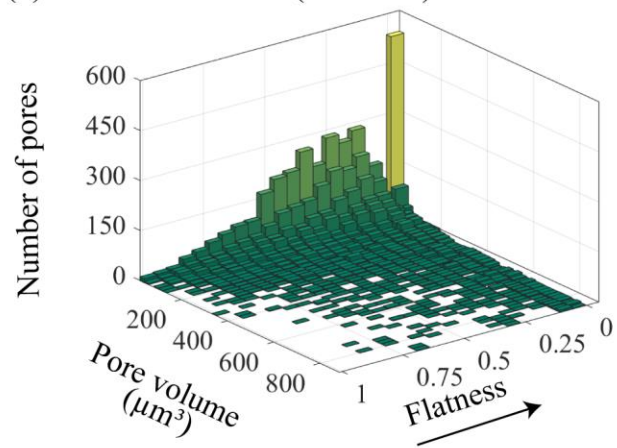
(b) DFDP-1B 69-2.48 (upper foliated ccl)



(c) DFDP-1B 69-2.54 (PSZ-2)



(d) DFDP-1B 69-2.57 (lower ccl)

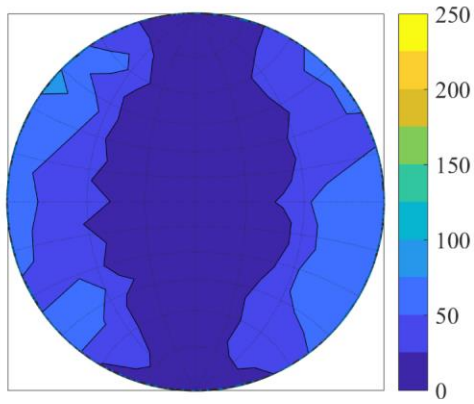


441

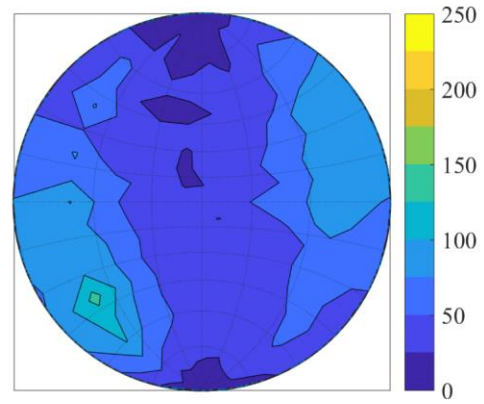
442 **Figure 6.** Bivariate histograms showing flatness versus pore volume (μm^3) and number of pores for each sample.

443 The arrow indicates the direction of increasing flatness.

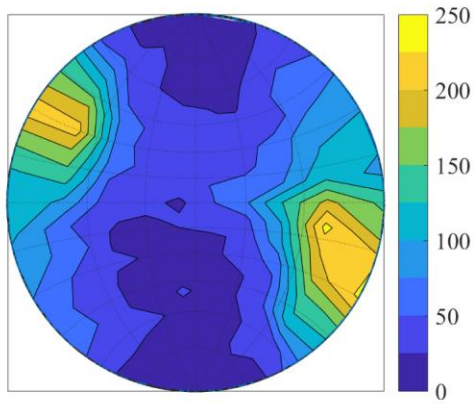
(a) DFDP-1B 58-1.9 (upper foliated ccl)



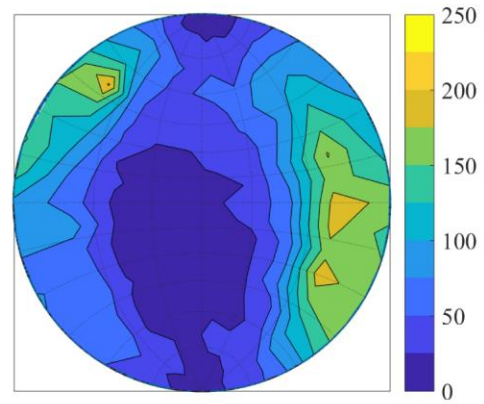
(b) DFDP-1B 69-2.48 (upper foliated ccl)



(c) DFDP-1B 69-2.54 (PSZ-2)



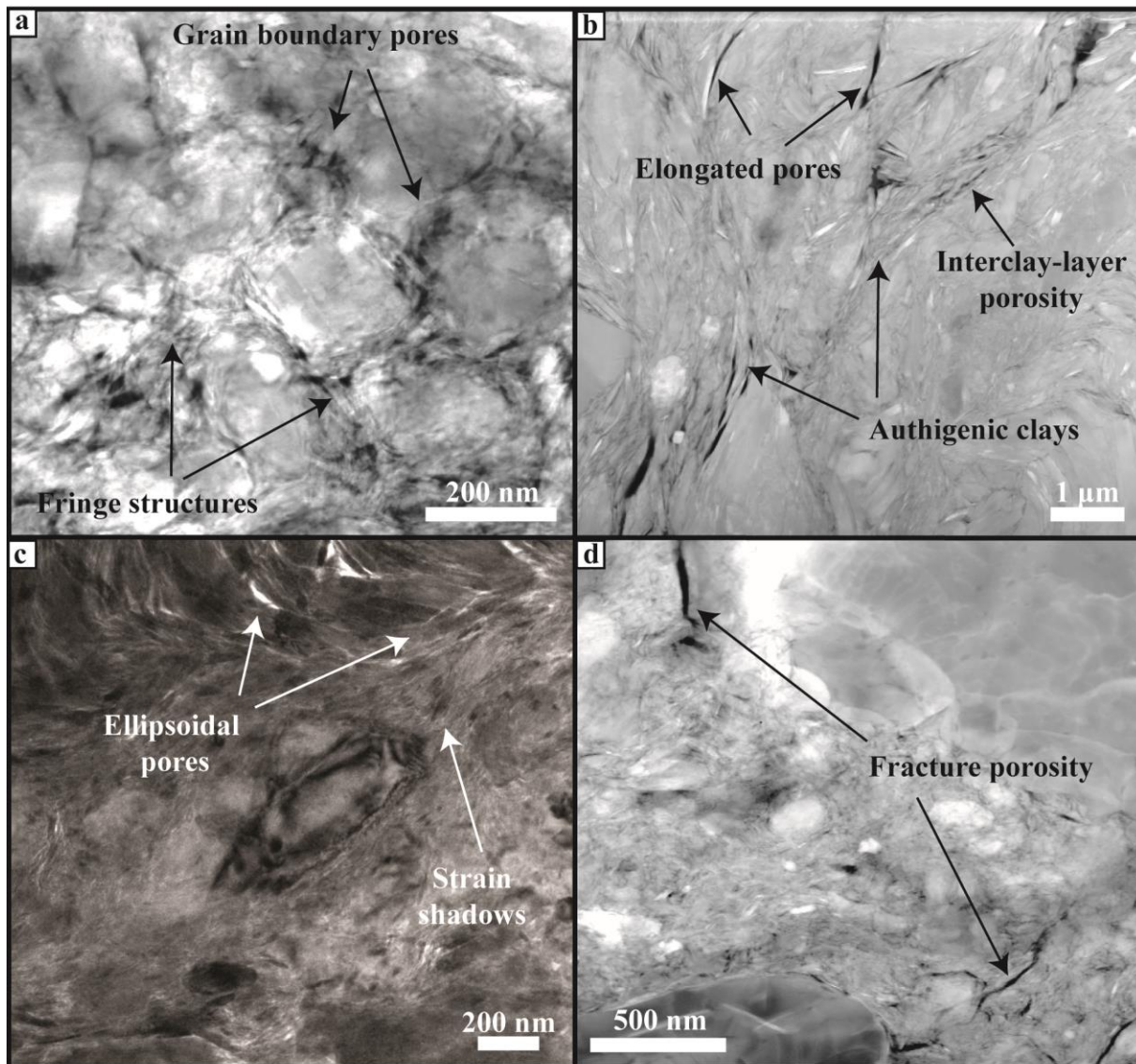
(d) DFDP-1B 69-2.57 (lower ccl)



444

445 **Figure 7.** Distribution of pore unit orientations plotted on a lower hemisphere equal area stereographic projection

446 with a probability density contour.



447
 448 **Figure 8.** Transmission electron microscopy images collected from the gouge sample DFDP-1B 69_2.54 (PSZ-2).
 449 (a) and (c) are bright-field images, where porosity appears as bright contrast areas. (b) and (d) are high-angle annular
 450 dark field images, where pores appear as dark contrasts areas. (a) TEM bright-field image of homogeneous fault
 451 gouge area. Quartz/feldspar grains, wrapped by fine authigenic clays, displaying fringe structures. Pores with sub-
 452 angular shape distributed along grain boundaries. (b) HAADF image of phyllosilicate-rich gouge area. Co-existence
 453 of fine authigenic clays with coarser clay mineral grains. Elongated pores and interlayer porosity. (c) TEM bright-
 454 filed image of ellipsoidal pores in phyllosilicate-rich areas. Examples of strain shadows along quartz/feldspar grains.
 455 (d) HAADF image of fracture porosity along grain boundaries of quartz/feldspar grains.